Research Square

Preprints are preliminary reports that have not undergone peer review.
They should not be considered conclusive, used to inform clinical practice,
or referenced by the media as validated information.

Coupled structural evolution and elemental redistribution in zigzag Pt3Fe nanowires revealed by in situ electrochemical liquid-cell TEM

Judith C. Yang

jyang1@bnl.gov

Brookhaven National Laboratory https://orcid.org/0000-0003-3936-3864

Meng Li

Brookhaven National Laboratory https://orcid.org/0000-0002-2745-4016

Jiawei Wan

University of California, Berkeley https://orcid.org/0000-0002-3805-5133

Ershuai Liu

Lawrence Berkeley National Laboratory https://orcid.org/0000-0002-6491-5504

Xuan Hu

University of California, Berkeley

Jiana Zheng

University of California, Berkeley

Kim Kisslinger

Brookhaven National Laboratory

Walter Drisdell

Lawrence Berkeley National Laboratory https://orcid.org/0000-0002-8693-4562

Shaofan Li

University of California, Berkeley https://orcid.org/0000-0002-6950-1474

Fang Lu

Brookhaven National Lab https://orcid.org/0000-0003-3765-7615

Haimei Zheng

Lawrence Berkeley National Laboratory https://orcid.org/0000-0003-3813-4170

Article

Keywords:

Posted Date: October 9th, 2026

DOI: https://doi.org/10.21203/rs.3.rs-11050251/v1

License: This work is licensed under a Creative Commons Attribution 4.0 International License.
Read Full License

Additional Declarations: There is **NO** Competing Interest.

Abstract

Shape and compositional control are widely used to tailor electrocatalyst properties, yet how these deliberately engineered features evolve under operating conditions remains poorly understood, obscuring the relationship between the as-synthesized catalyst and its active state. Here, we directly track the evolution of shape-controlled zigzag Pt_3Fe nanowires during the hydrogen evolution reaction under weakly alkaline conditions using *in situ* electrochemical liquid-cell transmission electron microscopy (EC-TEM), complemented by *in situ* X-ray absorption spectroscopy (XAS), elemental analysis, electron tomography, and electrostatic simulations. *Operando* EC-TEM reveals that the initially well-defined zigzag nanowires undergo spatially heterogeneous morphological evolution, including protrusion growth and nanoparticle formation preferentially at high-curvature regions. Correlated elemental mapping reveals selective Fe depletion and the formation of Pt-rich surface structures, while *in situ* XAS reveals increased Pt–Pt and decreased Pt–Fe coordination together with changes in the Fe chemical environment under HER conditions. Three-dimensional electron tomography resolves the zigzag nanowires as thin, plate-like structure rather than the previously proposed spiral-like geometry. Electrostatic simulations based on the experimentally determined geometry reveal electrostatic heterogeneity at high-curvature regions, providing a possible link between the nanowire geometry and the spatial preference of the observed morphological evolution. Together, these findings reveal coupled morphological evolution and elemental redistribution in shape-controlled alloy catalysts during electrochemical reactions. More broadly, these findings establish catalyst morphology as a dynamic parameter that not only defines the initial structure but also influences its subsequent evolution, highlighting dynamic structural evolution as an integral component of structure–property relationships in multicomponent electrocatalysts.

Introduction

Electrocatalysis offers a promising pathway toward sustainable and fossil-free production of fuels and chemicals by enabling hydrogen evolution, oxygen reduction, and other electrochemical redox reactions under mild conditions[1, 2]. The performance of electrocatalysts is intrinsically governed by their atomic composition and structural morphology, motivating extensive efforts to engineer materials with enhanced activity, selectivity, and stability[3, 4, 5]. Establishing reliable relationships between catalyst structure and catalytic properties is therefore central to the rational design of electrocatalytic materials.

Such structure–property relationships, however, are complicated by the highly dynamic nature of electrochemical interfaces. Catalyst surfaces can continuously evolve under the coupled influences of applied potential, electrolyte, and adsorbates[6, 7, 8, 9]. While surface restructuring has been extensively investigated in gas-phase catalytic systems[10, 11], directly probing dynamic structural evolution in liquid-phase environments remains challenging due to the complexity of solid-liquid interfaces and the transient nature of electrochemical processes[12, 13, 14]. Since these dynamic structural transformations

can strongly impact catalyst performance, identifying the active structure and composition of electrocatalysts under operating conditions remains a critical challenge[15].

Shape and composition engineering have emerged as two powerful and complementary approaches for tuning catalyst properties[3, 16]. Shape-controlled nanostructures expose well-defined crystal facets and high-curvature sites that enhance catalytic performance[17, 18, 19], while alloying leverages electronic and geometric effects to tune adsorption energetics and reaction pathways[20, 21]. However, despite their widespread use, how these two deliberately engineered features evolve together under operating conditions remains largely unexplored[5, 22]. Although liquid-cell TEM has been used to reveal dynamic transformations in alloy nanomaterials, such as dealloying and corrosion[14], electrochemical liquid cell TEM investigation on alloy catalysts remains scare[23, 24], and correlating morphological evolution with the accompanying elemental redistribution during electrocatalytic reactions remains challenging. This gap is particularly important for shape-controlled bimetallic catalysts, where both morphology and composition are deliberately engineered to enhance catalytic properties, raising a fundamental question of whether the initial nanoscale geometry also influences where and how the catalyst evolves under reaction conditions.

Shape-controlled Pt-based alloy electrocatalysts provide an important example of material systems in which both morphology and composition are deliberately engineered together to enhance electrocatalytic performance. In particular, zigzag Pt-M (M = transition metal) nanowires have emerged as a class of highly efficient electrocatalysts for a range of reactions, including the oxygen reduction reaction (ORR)[18, 20], hydrogen evolution reaction (HER)[25], and alcohol electro-oxidation reactions (EOR)[19, 26]. Their distinctive morphology, featuring periodic high-index facets and abundant high-curvature regions, offers a high density of active sites and unique local environments that can enhance catalytic activity[18, 19, 26, 27]. Such heterogeneous curvature of the zigzag morphology may also generate spatial variations in the local electrochemical environment, potentially influencing reaction kinetics, elemental stability, and structural evolution during operation.

Alloying Pt with transition metals offers an additional route to tune catalytic performance[25, 28]. While Pt exhibits excellent HER activity in acidic conditions, its performance in alkaline and neutral environments is significantly limited by the sluggish kinetics of H_2O dissociation[25]. Incorporation of Fe into Pt to form Pt_3Fe has been shown to substantially improve HER activity across a wide pH range[25]. This enhancement is attributed to the synergistic roles of Pt and Fe, where Pt preferentially binds hydrogen intermediates (H*) and Fe facilitates hydroxyl (OH*) adsorption[20, 28], thereby lowering the energy barrier for water dissociation and promoting subsequent hydrogen evolution. Despite extensive studies of the catalytic properties and as-synthesized structures of zigzag Pt-based alloy nanowires[18, 19, 26, 27], how their deliberately engineered morphology and alloy composition evolve under electrochemical operating conditions remains poorly understood[3, 6, 15, 22, 29]. Directly probing this coupled evolution requires *in situ/operando* characterization techniques capable of simultaneously resolving nanoscale morphology

evolution, elemental redistribution, and local electronic structure in liquid-phase electrochemical environments.

In this work, we investigate the coupled evolution of morphology and composition in shape-controlled zigzag Pt_3Fe nanowires during HER under weakly alkaline conditions. By integrating *in situ* electrochemical liquid-cell transmission electron microscopy (EC-TEM), three-dimensional (3D) electron tomography, synchrotron-based *in situ* X-ray absorption spectroscopy (XAS), and electrostatic simulations, we directly visualize morphological evolution, track elemental redistribution, and probe local electronic and coordination environments at the nanoscale. We reveal spatially heterogeneous morphological evolution preferentially localized at high-curvature regions of the zigzag nanowires, accompanied by selective Fe dealloying, Pt redistribution, and the formation of Pt-rich surface structures. Electron tomography further resolves the zigzag nanowires as thin, plate-like structures rather than the previously proposed spiral-like geometry, providing an experimentally determined 3D morphology for electrostatic simulations. The simulations reveal local electric-field enhancement at high-curvature regions, providing a possible link between the nanowire geometry and the spatial preference of the observed morphological evolution. Together, these findings reveal coupled morphological evolution and elemental redistribution in a shape-controlled alloy catalyst under electrochemical operating conditions.

Results and discussion

In situ EC-TEM setup and structure of zigzag Pt_3Fe nanowires

To directly investigate Pt_3Fe structural evolution under electrocatalytic conditions, *in situ* EC-TEM is performed using the electrochemical liquid-cell with a three-electrode configuration shown in Fig. 1a-c. Pt_3Fe nanowires are drop-cast onto the working electrode (WE), and the liquid-cell is equipped with a pressure-driven flow channel to precisely control the liquid thickness near the observation window, enabling more accurate measurements of the applied potential[30].

Figure 1d shows a representative Pt_3Fe nanowire with the characteristic zigzag morphology with periodically distributed convex and concave corners. The nanowires have an average width of ~ 20 nm and length ranging from 200 to 500 nm. The convex corners have an average angel of 75 ~ 80˚, and the average saw-to-saw distance is ~ 10 nm.

The composition and crystal structure of the pristine nanowires are further characterized by energy dispersive spectroscopy (EDS) and high-resolution (HR) TEM. EDS elemental mapping reveals a uniform Pt-Fe distribution, with an average Pt:Fe ratio of 3:1 (Fig. 2a). HRTEM shows the Pt_3Fe nanowire is single-crystalline, with a zone axis of [001] from the top-down direction (Fig. 2d). Corresponding fast-Fourier Transform (FFT) pattern shows superlattice spots at the middle of FCC diffraction spots, suggesting the as-synthesized nanowire has an ordered $L1_2$ alloy structure.

Together, we establish the initially homogeneous and structurally ordered Pt_3Fe alloy nanocatalyst, providing a well-defined reference for tracking the subsequent structural and compositional evolution under HER conditions on *in situ* platforms.

Operando observation of dynamic morphological reconstruction in zigzag Pt_3Fe nanowires

During the *operando* EC-TEM experiments, 0.1 M $KHCO_3$ solution is continuously flowed through the liquid-cell. After stabilization of electrolyte flow and electrical contact, a constant potential of V_{Pt}=-0.4 V is applied to the WE, selected based on the cyclic voltammetry (CV) response measured prior to the HER experiment (Fig. S1). The electrochemical current is recorded simultaneously with TEM imaging, allowing the morphological evolution of individual Pt_3Fe nanowires to be directly correlated with the corresponding electric response.

Under the applied potential, H_2 bubbles are observed to form on the nanowires, as evidenced by the sudden improvement in image clarity resulting from local thinning of the liquid layer, accompanied by the simultaneous sharp change in the measured current. Figure 3 presents a representative experiment in which several H_2 bubbles form intermittently during the application of the negative potential (blue shaded region in Fig. 3b), followed by rewetting as the liquid returned to the field of view. The time-series snapshots in Fig. 3c-g show enlarged frames of the region marked in Fig. 3a at selected bubble-formation events, corresponding to the current dips in Fig. 3b marked by colored circles, and the nanowire contours at different time points are outlined using corresponding colors. Overlaying these contours in Fig. 3h reveals spatially heterogeneous morphological evolution. The initially triangular protrusions progressively grow outward and, in some regions, split into two distinct peaks, accompanied by local deepening of neighboring concave valleys. These changes indicate localized mass redistribution and anisotropic morphological evolution under HER conditions.

Besides the large H_2 bubbles that temporarily thin the liquid across the entire field of view, HER continues within the remaining thin liquid layer, as evidenced by the gradual nucleation and growth of a smaller H_2 bubble between 46.5 s and 60 s (marked by circles, Fig. 3e-g). Notably, this bubble preferentially nucleates near a concave corner of the zigzag nanowire, and the neighboring nanowire segment also exhibits pronounced morphological evolution, suggesting a spatial association between local geometry, reaction environment, and nanowire evolution.

In situ visualization of Pt-rich nanoparticle nucleation and growth

In addition to the continuous reshaping of the zigzag morphology, *operando* EC-TEM reveals the nucleation and growth of discrete nanoparticles on the nanowire surface. Figure 4 shows a representative experiment in which a H_2 bubble forms and persists within the field of view throughout the applied negative bias. The persistent bubble substantially reduces the local liquid thickness, providing improved contrast for resolving nanoscale surface evolution while a residual liquid layer maintains electrochemical activity. The time-series snapshots in Fig. 4a reveal progressive morphological changes along the zigzag nanowire. Small nanoparticles gradually emerge on the

nanowire surface, initially appearing as subtle protrusions and subsequently developing into more distinct nanoparticles. These features preferentially nucleate at high-curvature regions along the zigzag edges and become increasingly distributed along the nanowire over time. The particle-position overlay in Fig. 4b further highlights the accumulation of these protrusions, indicating continuous surface morphological evolution under HER conditions.

Quantitative analysis of newly formed nanoparticles and their cumulative population in Fig. 4c indicates that nanoparticle nucleation is most active within the first ~ 10 s following the formation of the large H_2 bubble, after which the nucleation rate decreases significantly. Notably, although the number of nanoparticles increases during this period, their size remains relatively constant. In contrast, after the negative bias is removed, the large bubble disappears and the liquid layer thickens. Upon reapplying a negative potential and forming a new H_2 bubble, a pronounced increase in nanoparticle size is observed, suggesting that particle growth is favored under thicker liquid conditions (**Figure S2**).

Following nucleation, dynamic rotation and alignment of the nanoparticles are observed (Fig. 4d), resembling an oriented-attachment-like process[31]. This behavior is further supported by post-reaction HRTEM characterization (Fig. 2b, c), which shows that the nanoparticles share a similar crystallographic orientation with the Pt_3Fe nanowire substrate.

Compositional and crystallographic evolution of Pt_3Fe during HER

Having directly visualized the morphological evolution of Pt_3Fe nanowires under HER conditions, we next investigate the associated compositional and crystallographic evolution. To correlate these operando observations with post-reaction structure, the liquid was removed from the cell after different reaction durations, allowing the nanowires to be characterized by STEM-EDS and HRTEM and directly compared with the pristine material (Fig. 2). Compared with the homogeneous Pt–Fe distribution and ordered $L1_2$ structure of the pristine nanowires (Fig. 2a,d), pronounced compositional and structural changes are observed after HER (Fig. 2b,c,e,f).

After HER, substantial compositional redistribution becomes apparent in nanowires electrically connected to the working electrode (Fig. 2b). The Fe concentration within the nanowire decreases, while the newly formed surface nanoparticles are strongly enriched in Pt. EDS line profiles across the nanowire confirm Fe depletion from the alloy and Pt enrichment within the reconstructed surface features. EELS measurements of individual post-reaction nanoparticles further show no detectable Fe $L_{2,3}$ signal above the background (**Figure S3**), consistent with their strongly Fe-depleted, Pt-rich composition. In contrast, nanowires on the same substrate that are not electrically connected to the electrode retain their pristine zigzag morphology and Pt:Fe composition after exposure to the same electrolyte environment (**Figure S4**). This control confirms that the observed compositional and morphological evolution is associated with the electrochemical reaction rather than electrolyte exposure alone.

HRTEM reveals the corresponding crystallographic evolution (Fig. 2e). The newly formed Pt-rich nanoparticles preferentially appear at high-curvature regions of the nanowire and exhibit a crystallographic orientation similar to that of the underlying Pt_3Fe lattice. This observation is consistent with the dynamic rotational and alignment behavior observed during the in situ experiment (Fig. 4d), suggesting that the reconstructed Pt-rich structures retain a crystallographic relationship with the parent nanowire.

With prolonged HER operation, Fe depletion becomes substantially more pronounced (Fig. 2c and **Figure S5**), accompanied by the development of larger, dendrite-like Pt-rich structures along the nanowire surface. HRTEM shows that these structures maintain a similar crystallographic orientation to the underlying nanowire (Fig. 2f), possibly through the growth and coalescence of neighboring Pt-rich nanoparticles. Fe-containing deposits are also observed outside the nanowire after prolonged reaction, consistent with redistribution of Fe removed from the parent alloy (Fig. 2c).

In situ XAS reveals element-specific evolution during HER

To better understand the underlying chemical process, synchrotron-based *in situ* X-ray absorption spectroscopy (XAS) experiments are carried out on the same zigzag Pt_3Fe nanowire using a three-electrode liquid-cell. As shown in Fig. 5, clear potential-dependent trends are found in electronic states and local structure from both Pt L_3-edge and Fe K-edge under HER conditions.

At the Pt L_3 edge (Fig. 5a), the X-ray absorption near edge spectra (XANES) shows that the white-line intensity decreases from 0.54V to -0.2V vs. RHE, suggesting the formation of adsorbed hydrogen species ($Pt–H_{ad}$). The corresponding Fourier transform extended X-ray absorption fine structure (FT-EXAFS) spectra (Fig. 5b) exhibit relatively subtle changes; however, the increased peak intensity at ~ 2 Å indicates enhanced Pt–Pt interaction. To further deconvolute the Pt-Pt and Pt-Fe interactions under different electrochemical potentials, FT-EXAFS fittings are conducted to quantify the coordination number (CN) of Pt-Pt and Pt-Fe (**Figure S6, S7**). As shown in Fig. 5c, Pt-Fe alloy phase can be clearly identified in FT-EXAFS fittings. From OCV to -0.2V, the slight drop of the peaks of Pt-Fe path indicates the Pt_3Fe may go through dealloy under HER. Figure 5d shows that the CN of Pt-Pt increases from 9.6 to 10.6 meanwhile CN of Pt-Fe decreases from 1.8 to 1.5, consistent with TEM observed leaching of Fe and formation of Pt on the nanowire surface.

At the Fe K-edge, the XANES spectra (Fig. 5e) show a negative shift in the absorption edge along with more pronounced oscillation features after the major peaks, indicating progressive reduction of Fe species from OCV to HER conditions. This is further supported by the FT-EXAFS analysis (Fig. 5f), where the intensity of $Fe^0–Fe^0$ interactions at both the first (~ 2.2 Å) and second (~ 4.4 Å) coordination shells increase under more negative potentials, suggesting the formation of more metallic and bulk-like Fe domains. Combined with the EDS mapping results (Fig. 2), which shows Fe depletion from the nanowire, these findings suggest that Fe undergoes reduction and redistribution, likely accompanying leaching from the alloy and/or segregation into metallic domains.

Overall, the *in situ* XAS results reveal that under HER conditions, Pt sites are involved in hydrogen adsorption while Fe species are reduced and destabilized, driving compositional segregation. These chemical processes are consistent with TEM observations such as surface reshaping, Pt-rich nanoparticle formation, and Fe depletion from the nanowire.

Morphology-dependent reconstruction of zigzag Pt_3Fe nanowires

The spatially heterogeneous morphological evolution observed by *in situ* EC-TEM suggests that the initial zigzag geometry may influence how the nanowire evolves under reaction conditions. To understand the relationship between the zigzag morphology and this spatially selective reconstruction, the 3D structure of the Pt_3Fe nanowire was determined by tilt-series electron tomography combined with machine-learning-enhanced reconstruction[32] (Fig. 6a, **Figure S8**). The reconstruction reveals a thin, plate-like geometry with an average thickness of ~ 6 nm, rather than the previously proposed spiral-like structure[18]. This experimentally determined 3D morphology was subsequently used to construct a finite-element electrostatic model. The finite-element analysis reveals a strongly heterogeneous electrostatic environment along the zigzag nanowire, characterized by enhanced electric-field magnitude near the concave valleys and elevated electric potential near the convex regions (Fig. 6b, **Figure S9**). Interestingly, these regions exhibit distinct modes of morphological evolution during *in situ* EC-TEM, with progressive valley deepening accompanied by the formation of Pt-rich protrusions at the convex regions (Fig. 3h). Although the detailed relationship between the local electrostatic environment and these structural changes requires further investigation, the spatial correspondence suggests that the three-dimensional zigzag morphology may influence the local electrochemical environment and contribute to the anisotropic morphological evolution observed by *in situ* EC-TEM.

Chemical pathways of Fe removal and Pt redistribution

The combined XAS and EC-TEM results reveal distinct chemical responses of Pt and Fe under HER conditions. The decrease in Pt L_3-edge white-line intensity indicates increased hydrogen adsorption and the formation of Pt–H_{ad} species, while the negative shift of the Fe K-edge and increased Fe^0–Fe^0 coordination indicates reduction and redistribution of Fe. Together with the Fe depletion and Pt-rich surface structures observed by EDS, these results suggest coupled Fe removal and Pt redistribution during HER. Based on these observations, we propose the chemical pathways illustrated in Fig. 6c.

During HER in 0.1 M $KHCO_3$, cathodic water reduction generates adsorbed hydrogen and OH^-, producing a reducing and locally alkaline interface[33]. The observed decrease in surface Fe content, together with the Fe-containing deposits detected by EDS (Fig. 2c), indicates preferential Fe removal from Pt_3Fe. Interfacial K^+ may further facilitate this process through cation-assisted cathodic corrosion, analogous to that reported for Cu in the same electrolyte[12]. Once removed from the alloy, Fe species undergo hydrolysis and complexation with HCO_3^-/CO_3^{2-}. The increase in local pH shifts the bicarbonate–carbonate equilibrium towards CO_3^{2-} and favors the deposition of poorly soluble Fe

hydroxide/oxyhydroxide and carbonate phases[33, 34, 35, 36]. Such chemical trapping suppresses Fe reincorporation and consequently promotes the formation of a Pt-enriched surface.

Concurrently, the Pt-rich regions become highly hydrogen-covered, consistent with the PtH$_x$-like state indicated by our XAS results. At sufficiently negative potentials, multilayer surface and subsurface hydrogen can produce highly H-coordinated Pt configurations and disrupt the near-surface Pt lattice[35, 37], while interfacial alkali cations transiently stabilize the resulting anionic Pt–hydride intermediates. Under continued cathodic polarization, these hydride-like species can undergo cathodic dissolution and subsequently discharge through reaction with water and/or adsorbed hydrogen, releasing H_2 and regenerating Pt^0 for local redeposition. Pt redistribution is therefore attributed to a hydride-mediated cathodic dissolution–redeposition cycle rather than to pH-induced PtH$_x$ oxidation.[38] The coupling of selective Fe removal, hydroxide/carbonate trapping and PtH$_x$-mediated Pt transport accounts for the formation of Pt-rich nanoparticles and protrusions, while local redeposition onto the residual nanowire may preserve their crystallographic registry. Overall, the elementally heterogeneous evolution of Pt_3Fe reflects the coupled effects of metal stability, hydrogen affinity, alkali-cation stabilization and anion-mediated precipitation.

Summary and conclusion

In summary, we directly visualize and elucidate the dynamic structural and compositional evolution of zigzag Pt_3Fe nanowires under mild alkaline HER conditions by combining *in situ* EC-TEM, HRTEM and STEM-EDS characterizations, *in situ* synchrotron-based XAS, electron tomography, and FEM-based electrostatic simulations. *Operando* EC-TEM reveals spatially heterogeneous morphological evolution, including protrusion growth, nanoparticle formation, and local reshaping of the zigzag morphology. Correlated EDS and EELS measurements show that these morphological changes are accompanied by selective Fe removal and Pt redistribution, leading to the formation of Pt-rich surface structures. *In situ* XAS results provide element-specific insights into Pt-H adsorption and Fe reduction, linking the observed structural transformation to underlying electrochemical processes. Electron tomography resolves the zigzag nanowires as thin, plate-like structures, while electrostatic simulations based on the experimentally determined 3D morphology further reveal a spatially heterogeneous electrostatic environment across the zigzag geometry. The spatial correspondence between this electrostatic heterogeneity and the distinct morphological evolution observed at convex and concave regions suggests a possible role of the initial nanowire geometry in its subsequent evolution.

More broadly, these findings demonstrate that shape and composition, although deliberately engineered as catalyst design parameters, can evolve together under operating conditions. Moreover, the initial nanoscale morphology may influence the pathway through which this evolution proceeds. This dynamic interplay between initial structure and subsequent evolution underscores the need to consider the operating state, rather than the as-synthesized structure alone, when establishing structure–property relationships in multicomponent electrocatalysts. The multimodal approach presented here, integrating

real-time imaging with *in situ* spectroscopy, electron tomography and modeling, provides a powerful platform for resolving these coupled structural and chemical transformations in liquid-phase electrochemical environments. Extending this approach to other shape-controlled alloy systems could enable quantitative correlations between local morphology, reaction environment, and restructuring pathways, ultimately informing strategies for controlling catalyst evolution under operating conditions.

Methods

Synthesis of the zigzag Pt_3Fe nanowires

The Pt_3Fe zigzag nanowires are synthesized using the following a reported method[18]. $Pt(acac)_2$ (10 mg), $Fe(acac)_3$ (3 mg), glucose (20 mg), CTAC (80 mg), and OAm (5 mL) were combined in a 20 mL vial. The mixture was ultrasonicated for 1 h until fully dissolved, yielding a clear solution. The vial was then placed in an oil bath maintained at 200°C and heated for 12 h, after which it was allowed to cool naturally to room temperature. The resulting product was collected by centrifugation (8000 rpm, 5 min) and washed three times with an ethanol/cyclohexane mixture. Finally, the purified nanocrystals were dispersed in cyclohexane for subsequent use.

Ex situ TEM

HAADF-STEM/EDS characterization of the zigzag Pt_3Fe nanowire before and after reaction is carried out using an FEI F200X Talos (S)TEM operating at 200 keV equipped with a SuperX EDS detector with a solid angle of 0.9 srad. HRTEM characterization of the Pt_3Fe nanowire is performed using an image aberration-corrected FEI Titan ETEM operating at 300 keV. The electrochemical chip was dried out to improve the resolution of the characterizations.

Electron tomography

Electron tomography on the Pt_3Fe nanowires was performed on a FEI F200X Talos (S)TEM operating at 200 keV. Pt_3Fe nanowires were drop-casted onto Cu mesh grids and mounted in a Fischione 2020 tomography holder. Tilt-series images were collected in HAADF-STEM mode with a convergence angle of 10.5 mrad and a camera length of 205 mm. HAADF-STEM images (2048 × 2048 pixels) were recorded at 2° tilt increments from − 60° to + 60° with a dwell time of 3 μs and pixel size of 107.2 pm. Because local bending of the grid caused shadowing and a reduced signal-to-noise ratio at the extreme tilts, only the images from − 58° to + 58° were used for 3D reconstruction of the morphology. The transformation of 2D projection data to a 3D volumetric result was performed sequentially across a few complementary software packages. Firstly, the alignment of projection frames from electron microscopy was performed using Tomviz (Tomviz 1.10, Kitware Inc. Tomviz.org) center of mass and cross correlation and ImageJ TurboReg plugin (http://bigwww.epfl.ch/thevenaz/turboreg/), respectively. Following alignment, we utilize Dubbed Perception Fused Iterative Tomography Reconstruction Engine (PFITRE) [32] for the

electron microscopy data. The visualization and segmentation of the electron microscopy dataset used Dragonfly (Dragonfly 2025.1, Object Research Systems (ORS) Inc.).

In situ EC-TEM

In situ electrochemical liquid cell TEM experiments on the Pt_3Fe nanowires were performed using a DENSsolutions Stream holder on FEI F200X Talos (S)TEM (with FEI Ceta CMOS camera) and FEI Titan ETEM (with Gatan K2 direct electron camera). Electrochemical liquid chips with Pt electrodes were used for the experiment. The Pt_3Fe nanowires were first dissolved in ethanol and sonicated, then drop-casted onto the working electrode of the electrochemical chip. The samples were then dried out overnight to maximize the electric contact with the electrodes and avoid sample been wiped away under flowing electrolyte. 0.1 M $KHCO_3$ electrolyte was continuously flowed through the liquid cell during the *in situ* experiment. Prior to HER experiments, open-circuit potential (OCP) measurements and cyclic voltammetry (CV) scans were performed to confirm the electrolyte covered the entire electrodes region and good electrical contact between the sample and the electrodes have been established. During the in situ experiment, a constant negative potential (V_{Pt} = -0.4 ~ -0.6 V) was applied to the sample, selected based on the peak positions observed in the CV scans (**Figure S1**). To minimize the e-beam effect on the observation results, the electron dose was kept at the minimal level necessary for imaging, and the electron beam was blanked between acquisitions. The *in situ* data are taken at 2K by 2K resolution with an exposure time of 0.5 s.

In situ XAS

The Pt_3Fe catalyst was spray coated for XAS experiments. The electrode inks for the XAS electrodes were composed of 18.2 MΩ purity deionized water (Millipore), 2-propanol (HPLC-grade, Aldrich), 5 wt% EW1100 Nafion solution (Aldrich), and the synthesized catalyst powder. The ink was hand-painted onto a Sigarect 39BB carbon paper. The final Pt loading is around 0.2–0.4 mg/cm^2. The *in situ* XAS experiments were conducted at room temperature in a homemade spectro-electrochemical half-cell made of PEEK, with 0.1 M $KHCO_3$ electrolyte purged with N_2. The catalyst-impregnated samples were conditioned in the electrolyte under vacuum for 45 min to remove surface oxides and contaminants before transferring to the PEEK cell. Potentiostat control was maintained with a BioLogic potentiostat. The voltage cycling limits were 0.05–1.1 V (*vs.* RHE, for all *in situ* experiments) when collecting data at the Pt L_3-edge and Fe K-edge. The electrode was cycled between 0.05V and 1.2V to clean the Pt surface. Before each measurement, the cell was held for 5 min to reach a pseudo-steady state. Data collection was then performed at the chosen potentials held during anodic sweeps. All the experimental data were collected in conjunction with the corresponding reference foils to aid in energy alignment and normalization.

The data were processed and fit using the IFEFFIT-based Athena[39] and Artemis[40] programs. Scans were calibrated, aligned, normalized, and background corrected, using the IFEFFIT suite[41]. The χ(R) were modeled using single scattering paths calculated by FEFF6[42].

Finite-element-method (FEM) based numerical analysis

A three-dimensional electrostatic finite-element model was constructed in COMSOL Multiphysics. The model geometry is defined as $40 \times 20 \times 4$ nm and consists of a Pt_3Fe nanostructure embedded in a surrounding dielectric domain. The dielectric environment is represented by a rectangular block of characteristic size 50 nm. The Pt_3Fe region is assigned a uniform relative permittivity of $\epsilon_r = 1$, while the surrounding environment is assigned $\epsilon_r = 78.3$, corresponding to a water-like dielectric medium. A voltage terminal boundary is applied to the central surfaces inside Pt_3Fe, with the value set to 0.4 V. Ground boundary conditions are applied on the exterior boundaries of the surrounding dielectric domain. The remaining boundaries use the default electrostatic insulation condition. The domain is discretized using COMSOL's automatically generated tetrahedral mesh. A stationary study is used, and the solution is computed with a fully coupled stationary solver using an iterative linear solver with multigrid preconditioning.

Declarations

Author contributions

J. Y and H. Z initiated and supervised this project. M.L. performed the in situ ECTEM and ex situ HRTEM, EDS, EELS experiments. J.W. contributed to the initial conception of this study, synthesized the zigzag Pt_3Fe nanowires, and contributed to establishing the electrochemical reaction conditions, E. L. and J.W. performed the in situ XAS experiments. E.L. performed the XAS analysis. X. H. performed the electrostatic simulations, J. Z. contributed to the development of the proposed mechanism, K.K, M. L and F.L. performed the 3D electron tomography experiment, and F.L. performed the electron tomography reconstruction. M.L. analyzed and integrated the experimental results, developed the scientific interpretation, and drafted the initial manuscript. All authors discussed the results and reviewed and edited the manuscript.

Acknowledgements

This work was supported by U.S. Department of Energy Office of Science User Facility, at Brookhaven National Laboratory under Contract No. DE-SC0012704, and the U.S. Department of Energy, Office of Science, Office of Basic Energy Sciences (BES), Materials Sciences and Engineering Division under contract no. DE-AC02-05-CH11231 within the in situ TEM program (KC22ZH). This research used Electron Microscopy resources of the Center for Functional Nanomaterials (CFN), which is a U.S. Department of Energy Office of Science User Facility, at Brookhaven National Laboratory under Contract No. DE-SC0012704. M.L., F.L. and J.Y. were supported by DE-SC0012704. J.W., J.Z. and H.Z. were supported by DE-AC02-05-CH11231 under KC22ZH program. E.L. and W.S.D. were supported by the Liquid Sunlight Alliance, which is supported by the U.S. Department of Energy, Office of Science, Office of Basic Energy Sciences, Fuels from Sunlight Hub under Award No. DE-SC0021266. X. H was supported by

Professor T. Y. Lin Fellowship. This research used beamline 7-BM (QAS) of the National Synchrotron Light Source II, a U.S. Department of Energy, Office of Science User Facility operated by Brookhaven National Laboratory under Contract No. DE-SC0012704. Dr. Xueru Zhao at Brookhaven National Laboratory is gratefully acknowledged for performing the bench-top electrochemical measurements.

References

1. Zhu P, Wang HT (2021) High-purity and high-concentration liquid fuels through CO electroreduction. Nat Catal 4:943–951
2. Kattel S, Ramirez PJ, Chen JG, Rodriguez JA, Liu P (2017) Active sites for CO(2) hydrogenation to methanol on Cu/ZnO catalysts. Science 355:1296–1299
3. Cui C, Gan L, Heggen M, Rudi S, Strasser P (2013) Compositional segregation in shaped Pt alloy nanoparticles and their structural behaviour during electrocatalysis. Nat Mater 12:765–771
4. Porter NS, Wu H, Quan Z, Fang J (2013) Shape-control and electrocatalytic activity-enhancement of Pt-based bimetallic nanocrystals. Acc Chem Res 46:1867–1877
5. Zhao S, Yang Y, Tang Z (2022) Insight into Structural Evolution, Active Sites, and Stability of Heterogeneous Electrocatalysts. Angew Chem Int Ed Engl 61:e202110186
6. Yoon A et al (2025) Revealing catalyst restructuring and composition during nitrate electroreduction through correlated operando microscopy and spectroscopy. Nat Mater 24:762–769
7. Zhang Q et al (2024) Atomic dynamics of electrified solid–liquid interfaces in liquid-cell TEM. Nature 630:643–647
8. Yang Y et al (2024) Dynamic Evolution of Copper Nanowires during CO(2) Reduction Probed by Operando Electrochemical 4D-STEM and X-ray Spectroscopy. J Am Chem Soc 146:23398–23405
9. Shen TH, Girod R, Tileli V (2023) Insights into Electrocatalyst Transformations Studied in Real Time with Electrochemical Liquid-Phase Transmission Electron Microscopy. Acc Chem Res 56:3023–3032
10. Li M, Curnan MT, Saidi WA, Yang JC (2022) Uneven Oxidation and Surface Reconstructions on Stepped Cu(100) and Cu(110). Nano Lett 22:1075–1082
11. Lee Y et al (2025) Machine-Learning-Driven Exploration of Surface Reconstructions of Reduced Rutile TiO2. Angewandte Chemie - Int Ed 64:1–39
12. Liu S et al (2024) Alkali cation-induced cathodic corrosion in Cu electrocatalysts. Nat Commun 15:5080
13. Amirbeigiarab R et al (2023) Atomic-scale surface restructuring of copper electrodes under CO2 electroreduction conditions. Nat Catal 6:837–846
14. Zheng J, Zhang Q, Lee D, Chen Y, Bustillo KC, Zheng H (2026) Heterogeneous Corrosion Pathways in Pt–Ni Nanododecahedra Revealed by In Situ Liquid Cell TEM. Nano Lett 26:1313–1320
15. Li M, House SD, Yang JC (2025) Deciphering electrocatalysts with multimodal operando approaches. Nat Mater 24:664–665

16. Gasteiger HA, Markovic NM (2009) Chemistry. Just a dream–or future reality? Science 324:48–49
17. Li C, Clament Sagaya Selvam N, Fang J (2023) Shape-Controlled Synthesis of Platinum-Based Nanocrystals and Their Electrocatalytic Applications in Fuel Cells. Nanomicro Lett 15:83
18. Luo M et al (2018) Stable High-Index Faceted Pt Skin on Zigzag-Like PtFe Nanowires Enhances Oxygen Reduction Catalysis. Adv Mater 30:1–9
19. Bai S, Bu L, Shao Q, Zhu X, Huang X (2018) Multicomponent Pt-Based Zigzag Nanowires as Selectivity Controllers for Selective Hydrogenation Reactions. J Am Chem Soc 140:8384–8387
20. Gong M et al (2019) Optimizing PtFe intermetallics for oxygen reduction reaction: from DFT screening to in situ XAFS characterization. Nanoscale 11:20301–20306
21. Song TW et al (2022) Intermetallic PtFe Electrocatalysts for the Oxygen Reduction Reaction: Ordering Degree-Dependent Performance. Small 18:e2202916
22. Liu L, Corma A (2021) Structural transformations of solid electrocatalysts and photocatalysts. Nat Rev Chem 5:256–276
23. Beermann V, Holtz ME, Padgett E, de Araujo JF, Muller DA, Strasser P (2019) Real-time imaging of activation and degradation of carbon supported octahedral Pt–Ni alloy fuel cell catalysts at the nanoscale usingin situelectrochemical liquid cell STEM. Energy Environ Sci 12:2476–2485
24. Tan SF, Reidy K, Klein J, Pinkowitz A, Wang B, Ross FM (2021) Real-time imaging of nanoscale electrochemical Ni etching under thermal conditions. Chem Sci 12:5259–5268
25. Kuang P, Ni Z, Zhu B, Lin Y, Yu J (2023) Modulating the d-Band Center Enables Ultrafine Pt(3) Fe Alloy Nanoparticles for pH-Universal Hydrogen Evolution Reaction. Adv Mater 35:e2303030
26. Xu Y et al (2019) Highly active zigzag-like Pt-Zn alloy nanowires with high-index facets for alcohol electrooxidation. Nano Res 12:1173–1179
27. Bu L et al (2016) Surface engineering of hierarchical platinum-cobalt nanowires for efficient electrocatalysis. Nat Commun 7:11850
28. Wu Y, Yao J, Gao J (2020) Interface Chemistry of Platinum-Based Materials for Electrocatalytic Hydrogen Evolution in Alkaline Conditions. *Methods for Electrocatalysis*). Springer International Publishing
29. Zheng J, Zhang Q, Lee D, Chen Y, Bustillo KC, Zheng H (2026) Heterogeneous Corrosion Pathways in Pt-Ni Nanododecahedra Revealed by In Situ Liquid Cell TEM. Nano Lett 26:1313–1320
30. Beker AF et al (2020) In situ electrochemistry inside a TEM with controlled mass transport. Nanoscale 12:22192–22201
31. Li D, Nielsen MH, Lee JR, Frandsen C, Banfield JF, De Yoreo JJ (2012) Direction-specific interactions control crystal growth by oriented attachment. Science 336:1014–1018
32. Zhao C, Ge M (2025) With Machine-Learning Enabled Iterative Reconstruction Engine. 1–12
33. Lu X, Zhu C, Wu Z, Xuan J, Francisco JS, Wang H (2020) In Situ Observation of the pH Gradient near the Gas Diffusion Electrode of CO(2) Reduction in Alkaline Electrolyte. J Am Chem Soc 142:15438–15444

34. Jiang CZ, Tosca NJ (2019) Fe(II)-carbonate precipitation kinetics and the chemistry of anoxic ferruginous seawater. Earth Planet Sci Lett 506:231–242
35. Furcas FE, Mundra S, Lothenbach B, Angst UM (2024) Speciation Controls the Kinetics of Iron Hydroxide Precipitation and Transformation at Alkaline pH. Environ Sci Technol 58:19851–19860
36. Albert C, Mundra S, Furcas FE, Isgor OB, Angst U (2026) Steel corrosion in near-neutral pH electrolytes with bicarbonate, chloride, and sulfate ions. Electrochim Acta 546:147725–147725
37. Hersbach TJP et al (2025) Platinum hydride formation during cathodic corrosion in aqueous solutions. Nat Mater 24:574–580
38. Aarts M, Trindell JA, Koper MTM (2026) Disentangling effects of pH, potential, and cation concentration in cathodic corrosion of platinum. Phys Chem Chem Phys 28:1189–1195
39. Newville M, Livins P, Yacoby Y, Rehr JJ, Stern EA (1993) Near-edge x-ray-absorption fine structure of Pb: A comparison of theory and experiment. Phys Rev B Condens Matter 47:14126–14131
40. Ravel B, Gallagher K (2005) Atomic structure and the magnetic properties of Zr-doped Sm2Co17. Phys Scr T115:606–608
41. Newville M (2001) IFEFFIT: interactive XAFS analysis and FEFF fitting. J Synchrotron Radiat 8:322–324
42. Ankudinov AL, Ravel B, Rehr JJ, Conradson SD (1998) Real-space multiple-scattering calculation and interpretation of x-ray-absorption near-edge structure. Phys Rev B 58:7565–7576

Figures

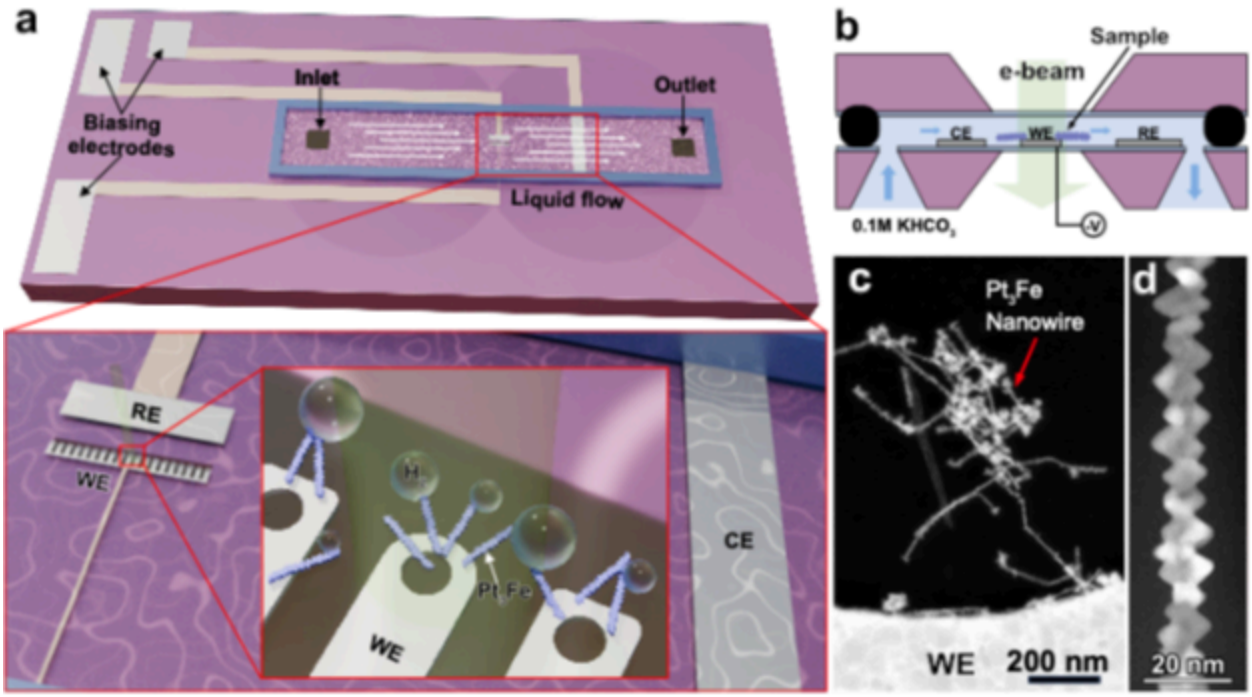

Figure 1

Experimental setup of *in situ* EC-TEM on zigzag Pt_3Fe nanowires. (a) Schematic illustration of the electrochemical liquid-cell chip, the magnified inset highlights the three-electrode configuration, including the working electrode (WE), reference electrode (RE), and counter electrode (CE), as well as the location of the zigzag Pt_3Fe nanowires. (b) Cross-section schematic of the electrochemical liquid-cell setup inside TEM, showing the liquid flow, electron beam path, and electric biasing applied to the sample. (c) Lower magnification HAADF-STEM image of the zigzag Pt_3Fe nanowires on a WE. Scale bar: 200 nm. (d) Higher magnification HAADF-STEM image of a single zigzag Pt_3Fe nanowire. Scale bar: 20 nm.

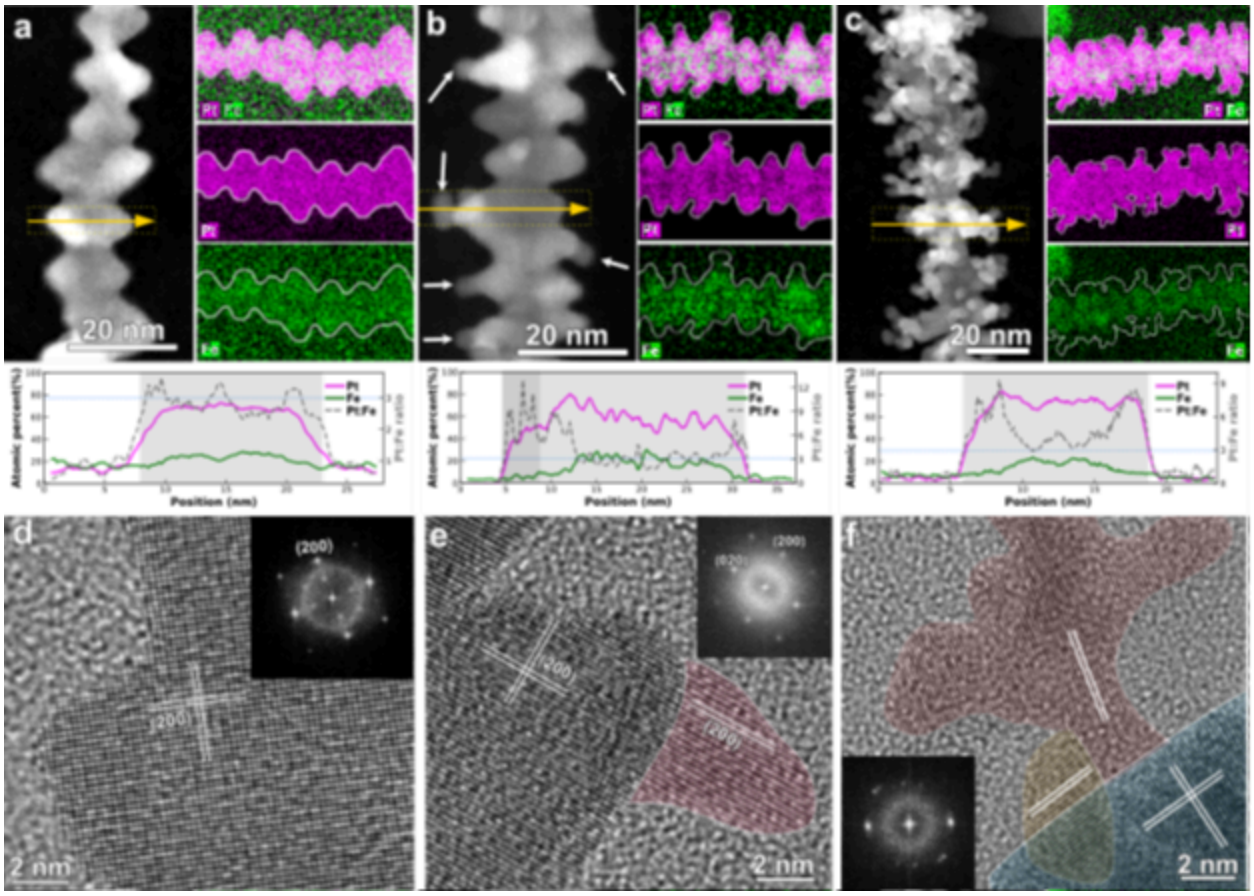

Figure 2

Structural and compositional evolution of zigzag Pt_3Fe nanowire during HER. (a-c) HAADF-STEM and corresponding EDX elemental maps (atomic percent) of the nanowires before (a), after (b) and after prolonged HER reaction (c). The plots below each panel show line-scan profiles extracted from the marked regions in the HAADF images, showing a gradual leaching of Fe (green) from the nanowire, and the newly formed particles are Pt (magenta) rich. (d-f) HRTEM image of the sample at the corresponding phases. (d) Pristine nanowire shows an ordered Pt_3Fe $L1_2$ structure, evidenced by the superlattice spots in the FFT inset. (d) After HER, Pt nanoparticle forms at the convex corner of the nanowire, showing an epitaxial orientation relationship with nanowire substrate. (e) After prolonged HER reaction, dendrite-like

Pt nanostructures form on the nanowire surface, these nanostructures maintain a similar orientation with the nanowire substrate.

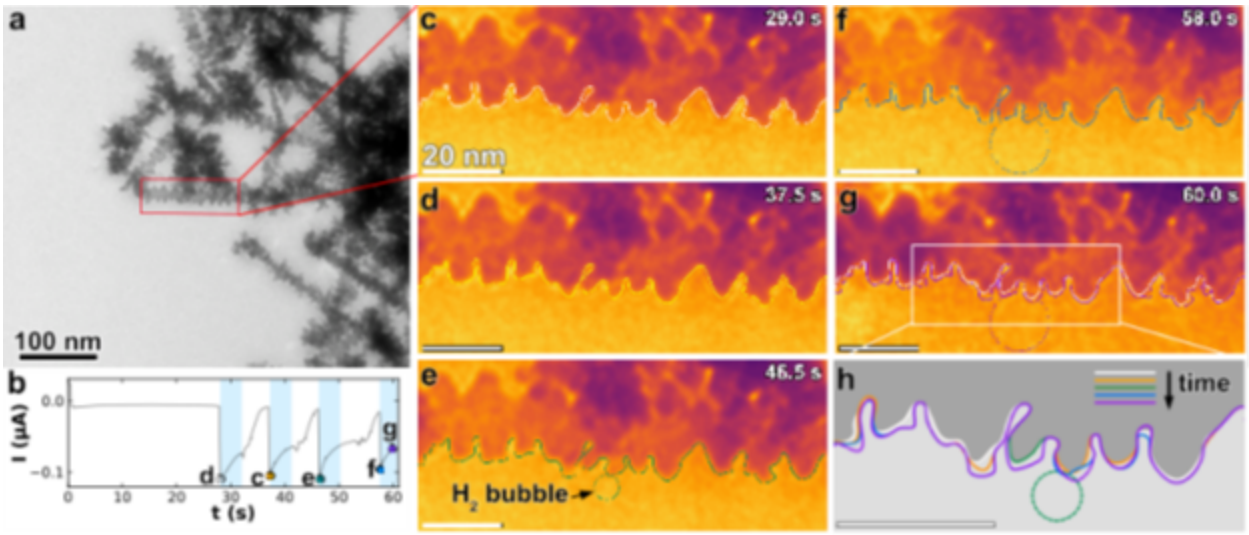

Figure 3

Spatially heterogeneous morphological evolution of zigzag Pt_3Fe nanowires during HER. (a) EC-TEM image showing the nanowire position, the WE is on the right of the nanowires (outside of view). (b) Corresponding electrochemical current recorded under constant applied potential of V_{Pt}= -0.4V. The shaded regions indicate H_2-bubble events associated with local thinning of the liquid layer, and the colored markers indicate the time points shown in (c–g). (c-g) Enlarged time-resolved EC-TEM images of the region marked in (a), showing progressive changes in the zigzag morphology. A small H_2 bubble is observed to nucleate and grow at the sharp corner of the nanowire at 46.5-60 s, further evidencing the HER reaction. (h) Overlay of nanowire contours extracted at different time points, revealing outward growth and splitting of convex protrusions accompanied by local deepening of neighboring concave valleys. Scale bar: 20 nm.

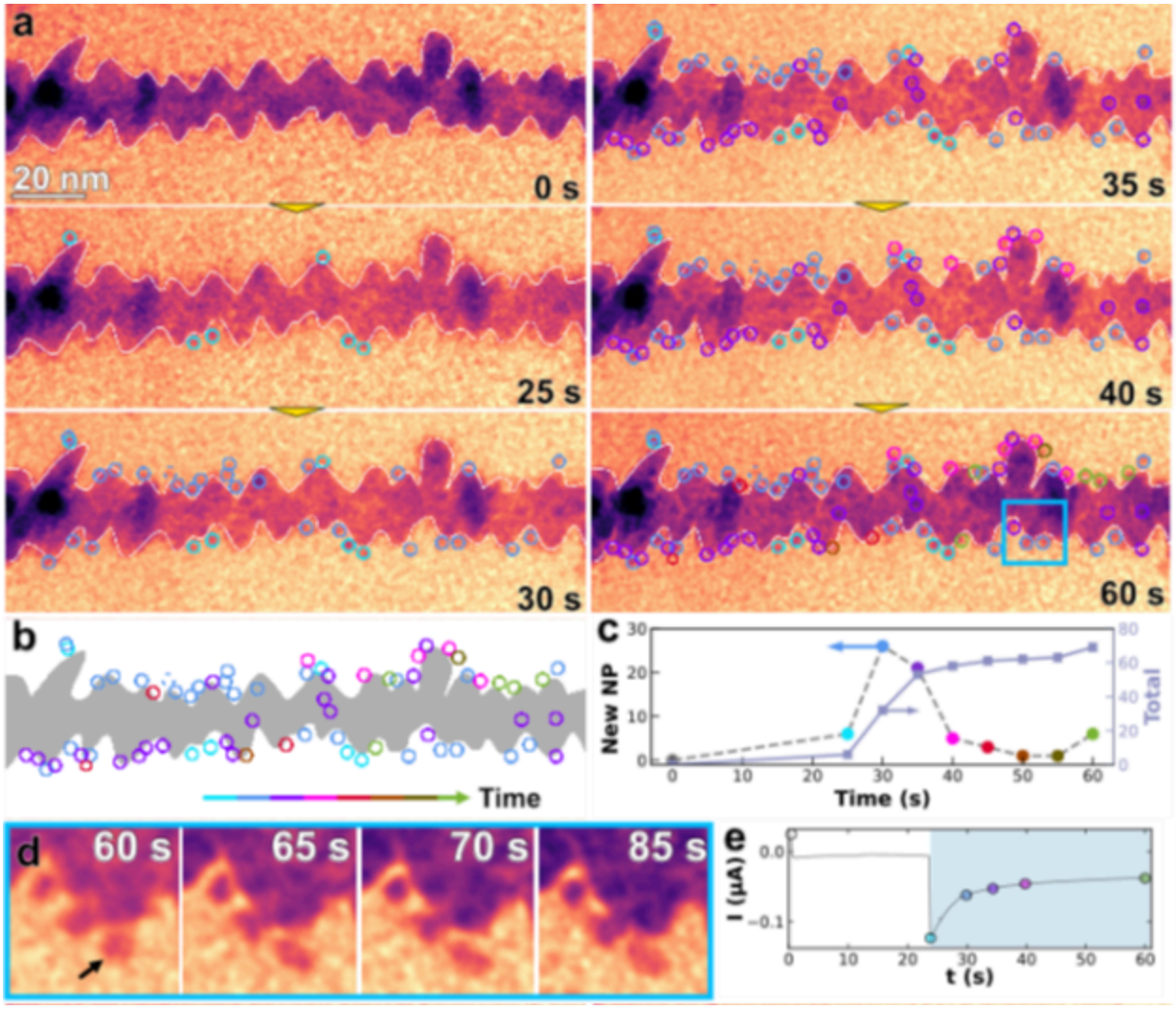

Figure 4

Operando visualization of nanoparticle nucleation and growth on zigzag Pt_3Fe nanowires. (a) Time-resolved EC-TEM images showing the progressive formation of nanoparticles along the nanowire surface. Newly identified nanoparticles are marked by circles, with colors indicating their time of appearance. (b) Overlay of nanoparticle positions identified at different time points, illustrating their spatial and temporal distribution along the nanowire. (c) Quantification of the number of newly formed nanoparticles at each time point (left axis) and the cumulative number of nanoparticles (right axis). (d) Enlarged view of the boxed region in (a), showing the oriented-attachment-like adjustment of the nanoparticle orientation during growth. (e) Corresponding electrochemical current recorded during the experiment. The shaded region indicates the period of a persistent H_2 bubble that leads to a thinner local liquid layer, and the colored markers correspond to the time points shown in (a–c).

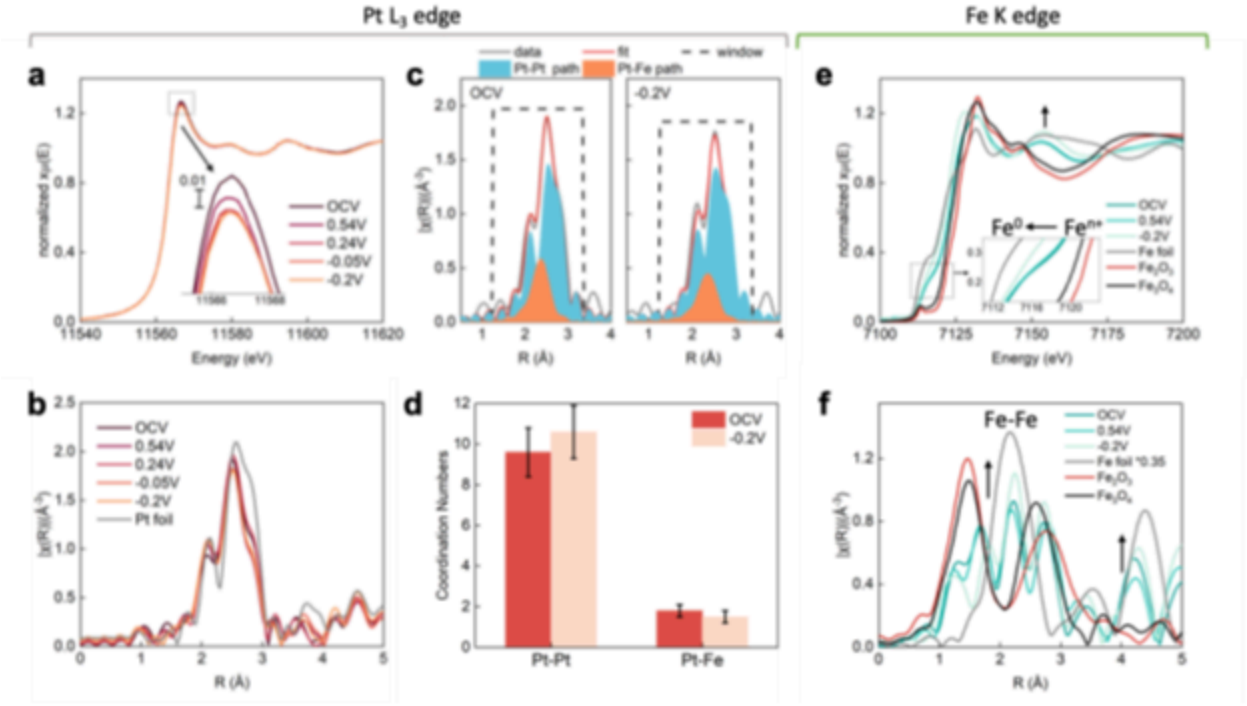

Figure 5

***In situ* XAS measurements of the Pt_3Fe nanowire in N_2-saturated 0.1 M $KHCO_3$.** (a) XANES spectra collected at Pt L_3-edge, the white line intensity (zoomed in as boxed region) decreases under negative bias, suggesting formation of Pt-H_{ad}. (b) FT-EXAFS spectra at Pt L_3-edge show mild changes under reaction conditions. The increased peak around 2Å indicates more Pt-Pt interactions, which is further verified by the FT-EXAFS fitting results, with deconvoluted Pt-Pt and Pt-Fe interactions shown in (c). (d) Summary of coordination number acquired from FT-EXAFS fittings under OCV and -0.2 V. (e) XANES at Fe K-edge, the negative shift of the edge and the more prominent oscillation features after the major peak indicate a reduction behavior of Fe sites from OCV to HER conditions. (f) FT-EXAFS at Fe K-edge, showing under more negative potential, the Fe^0-Fe^0 interactions at first shell (~2.2Å) and second shell (~4.4Å) increase, suggesting more formation of metallic Fe and bulky metallic Fe phase.

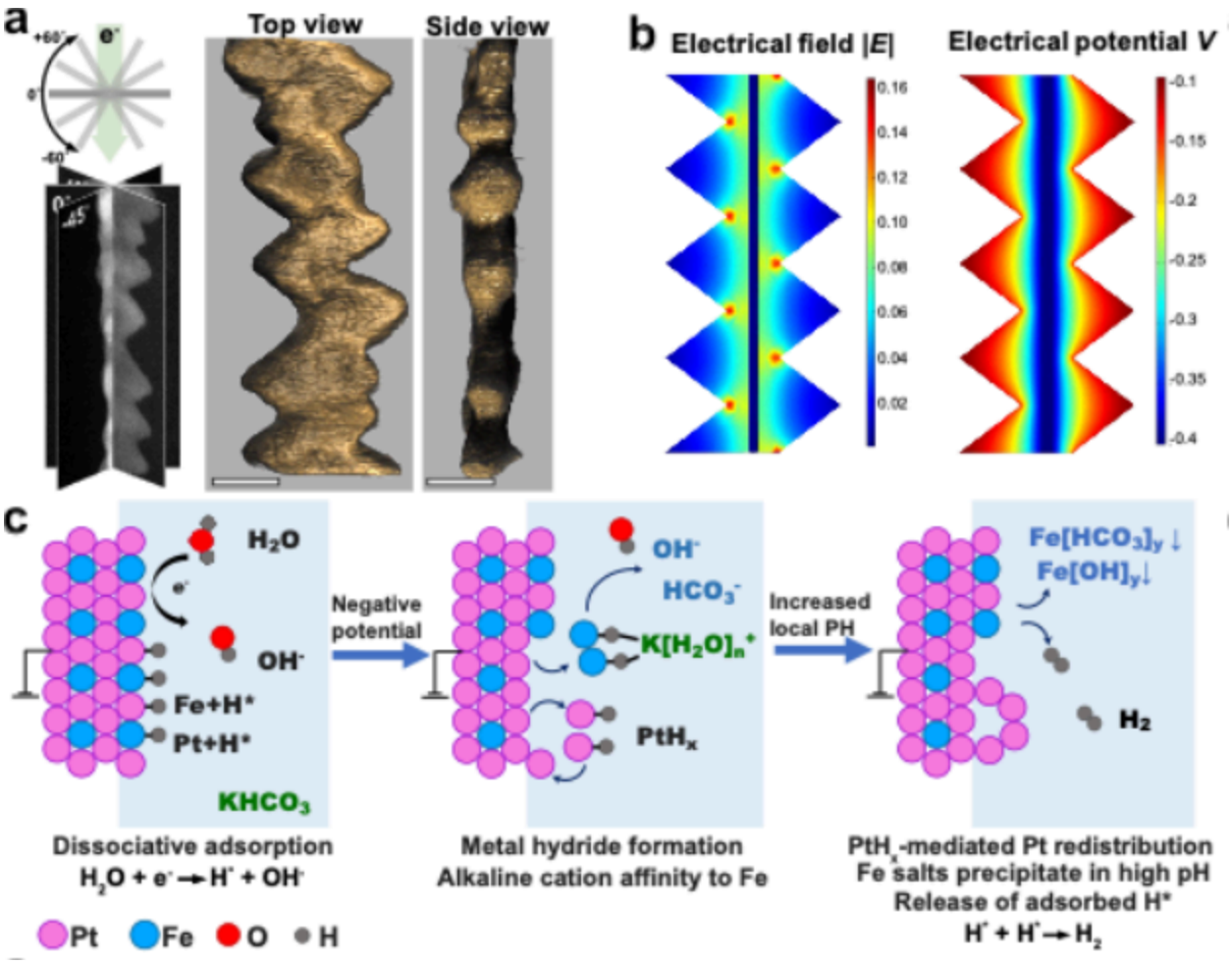

Figure 6

Electron tomography, electrostatic heterogeneity, and proposed mechanisms. (a) Tilt-series electron tomography reconstruction of the Pt_3Fe zigzag nanowire viewed along different orientations, revealing a thin, plate-like 3D morphology. (b) Finite-element electrostatic simulations based on the experimentally determined 3D morphology, showing the distributions of electric-field magnitude (left) and electric potential (right). The simulations reveal enhanced electric-field magnitude near the concave valleys and elevated electric potential near the convex regions, demonstrating a spatially heterogeneous electrostatic environment associated with the zigzag morphology. (c) Proposed chemical pathways underlying the structural and compositional evolution of Pt_3Fe under HER conditions, involving hydrogen adsorption and PtH_x formation, Fe removal and precipitation, and Pt redistribution leading to Pt-rich surface structures.

Supplementary Files

This is a list of supplementary files associated with this preprint. Click to download.

- MovieS2.avi
- MovieS5Tomography.avi

- PtFeSIsubmit.docx
- MovieS4.avi
- MovieS1.avi
- MovieS3.avi